catalysts

MDPI

Article

Constructing Hydrazone-Linked Chiral Covalent Organic Frameworks with Different Pore Sizes for Asymmetric Catalysis

Haichen Huang †, Kai Zhang †, Yuexin Zheng, Hong Chen, Dexuan Cai, Shengrun Zheng, Jun Fan * and Songliang Cai *

GDMPA Key Laboratory for Process Control and Quality Evaluation of Chiral Pharmaceuticals, and Guangzhou Key Laboratory of Analytical Chemistry for Biomedicine, School of Chemistry, South China Normal University, Guangzhou 510006, China; 2023022485@m.scnu.edu.cn (H.H.); 2022010167@m.scnu.edu.cn (K.Z.); 20222421107@m.scnu.edu.cn (Y.Z.); 20232432016@m.scnu.edu.cn (D.C.); zhengsr@scnu.edu.cn (S.Z.)

* Correspondence: fanj@scnu.edu.cn (J.F.); songliangcai@m.scnu.edu.cn (S.C.)

† These authors contributed equally to this work.

Abstract

Chiral covalent organic frameworks (COFs) hold great promise in heterogeneous asymmetric catalysis due to their designable structures and well-defined chiral microenvironments. However, precise control over the pore size of chiral COFs to optimize asymmetric catalytic performance remains challenging. Herein, we designed a proline-derived dihydrazide chiral monomer (*L*-DBP-Boc), which was subjected to Schiff-base reactions with two aromatic aldehydes of different lengths, 1,3,5-triformyl phloroglucinol (BTA) and 4,4′,4″-(1,3,5-triazine-2,4,6-triyl)tribenzaldehyde (TZ), to construct two hydrazone-linked chiral COFs with distinct pore sizes (*L*-DBP-BTA COF and *L*-DBP-TZ COF). Interestingly, the Boc protecting groups were removed in situ during COF synthesis. We systematically investigated the catalytic performance of these two chiral COFs in asymmetric aldol reactions and found that their pore sizes significantly influenced both catalytic activity and enantioselectivity. The large-pore *L*-DBP-TZ COF (pore size: 3.5 nm) exhibited superior catalytic performance under aqueous conditions at room temperature, achieving a yield of 98% and an enantiomeric excess (ee) value of 78%. In contrast, the small-pore *L*-DBP-BTA COF (pore size: 2.0 nm) showed poor catalytic performance. Compared to *L*-DBP-BTA COF, *L*-DBP-TZ COF demonstrated a 1.69-fold increase in yield and a 1.56-fold enhancement in enantioselectivity, possibly attributed to the facilitated diffusion and transport of substrates and products within the larger pore, thus improving the accessibility of active sites. This study presents a facile synthesis of pyrrolidine-functionalized chiral COFs and establishes the possible structure–activity relationship in their asymmetric catalysis, offering new insights for the design of efficient chiral COF catalysts.

Keywords: chiral covalent organic frameworks; different pore sizes; asymmetric catalysis

check for updates

Academic Editor: Daming Du

Received: 8 June 2025
Revised: 28 June 2025
Accepted: 29 June 2025
Published: 30 June 2025

Citation: Huang, H.; Zhang, K.; Zheng, Y.; Chen, H.; Cai, D.; Zheng, S.; Fan, J.; Cai, S. Constructing Hydrazone-Linked Chiral Covalent Organic Frameworks with Different Pore Sizes for Asymmetric Catalysis. *Catalysts* **2025**, *15*, 640. https://doi.org/10.3390/catal15070640

Copyright: © 2025 by the authors. Licensee MDPI, Basel, Switzerland. This article is an open access article distributed under the terms and conditions of the Creative Commons Attribution (CC BY) license (https://creativecommons.org/licenses/by/4.0/).

1. Introduction

Chiral covalent organic frameworks (COFs), a new type of crystalline chiral porous materials constructed through strong covalent bonds [1–3]. Owning to their high specific surface area, exceptional stability, and well-defined chiral active sites, chiral COFs have demonstrated remarkable potential in asymmetric catalysis [4–11], chiral recognition [12–18], enantiomer separation [19–25], and circularly polarized luminescence [26–31]. In the field of asymmetric catalysis, chiral COFs offer distinct advantages over traditional homogeneous small-molecule chiral catalysts. As heterogeneous catalysts, they can be easily recovered

and reused, exhibiting excellent recyclability. Moreover, the large pore volumes and open channels of chiral COFs facilitate efficient reactant diffusion and mass transfer, thereby enhancing the catalytic activity. Indeed, their framework structures and chiral microenvironments can be precisely tailored by modifying the organic building blocks, enabling the rational design of high-performance chiral COF catalysts. Consequently, chiral COFs have emerged as a fascinating class of catalytic materials, garnering widespread research interest in recent years [32–36].

Among the factors influencing the catalytic performance of chiral COFs, the pore environment is a critical determinant. Strategies such as incorporating diverse chiral building blocks and post-synthetic functionalization have been employed to modulate the pore microenvironments of chiral COFs, thereby enabling precise control over their asymmetric catalytic performance [9,32,37,38]. For instance, in 2019, Cui's group synthesized two chiral COFs with distinct functional chiral groups on the pore walls via a direct synthesis approach and investigated their potential in asymmetric Michael addition reactions [37]. The Wang group developed four chiral COFs by introducing different functional groups into the pores, creating a unique platform to explore structure–activity relationships in asymmetric catalysis through molecular atomic-level microenvironment tuning [32]. In 2024, Jiang and coworkers incorporated rhodium nanoparticles modified with chiral diene ligands into COF frameworks, where the tailored chiral microenvironments around the rhodium nanoparticles significantly improved the enantioselectivity in asymmetric reactions between arylboronic acids and nitroolefins [9]. Our group recently demonstrated that hydrazone-linked chiral COFs with varying densities of chiral sites in their pores markedly influence the catalytic performance in aldol reactions between cyclohexanone and 4-nitrobenzaldehyde [38]. Despite these advances in optimizing pore microenvironments to enhance catalytic performance, investigations on improving asymmetric catalysis by systematically varying the pore sizes of chiral COFs remain exceedingly rare. Addressing this knowledge gap will deepen the understanding of structure–performance relationships in chiral COFs and provide new insights for designing highly efficient asymmetric catalysts.

Herein, we designed and synthesized two hydrazone-linked chiral COFs featuring identical pyrrolidine chiral functional groups but distinct pore sizes, namely *L*-DBP-BTA COF (pore size: 2.0 nm) and *L*-DBP-TZ COF (pore size: 3.5 nm). Notably, the Boc protecting group could be removed in situ during COF synthesis, enabling a one-step, facile construction of pyrrolidine-functionalized chiral COFs. More importantly, when employed as heterogeneous catalysts in asymmetric aldol reactions, these chiral COFs exhibited pore-size-dependent catalytic activity and enantioselectivity. The large-pore *L*-DBP-TZ COF demonstrated superior performance, achieving 98% yield and 78% enantiomeric excess (ee), whereas the small-pore *L*-DBP-BTA COF displayed significantly lower efficacy. In comparison to *L*-DBP-BTA COF, *L*-DBP-TZ COF exhibited a 1.69-fold increase in yield and a 1.56-fold enhancement in enantioselectivity. This is primarily attributed to the larger pore size of the chiral *L*-DBP-TZ COF, which facilitate faster substrate access to chiral catalytic active sites and prompt release of the product, therefore enhancing the mass transfer efficiency of both substrates and products. Beyond offering a new strategy for enhancing the catalytic performance of chiral COFs, this work elucidates the critical role of pore size in asymmetric catalysis, providing new insights for the design of high-performance chiral COF catalysts.

2. Results and Discussion

2.1. Facile Synthesis of Pyrrolidine-Functionalized Chiral COFs

The Boc-protected chiral building block *L*-DBP-Boc was synthesized via the following steps: Firstly, Suzuki coupling of methyl 3-amino-4-bromobenzoate with (4-

(methoxycarbonyl)phenyl)boronic acid yielded an amino-functionalized biphenyl dimethyl dicarboxylate. This intermediate then underwent amide condensation with *L*-proline-Boc to form the *L*-Boc-pyrrolidine-containing biphenyl dimethyl dicarboxylate. Finally, the chiral monomer *L*-DBP-Boc was obtained through the hydrazidation reaction (Scheme S1). As illustrated in Figure 1, the chiral monomer *L*-DBP-Boc underwent Schiff-base condensation with 1,3,5-triformylphloroglucinol (BTA) in a mixture of degassed 6 M acetic acid aqueous solution/mesitylene/1,4-dioxane (1:6:2, *v*/*v*/*v*) at 110 °C for 3 days, yielding the small-pore pyrrolidine-functionalized *L*-DBP-BTA COF (yield: 72%). Similarly, reaction of *L*-DBP-Boc with 4,4′,4″-(1,3,5-triazine-2,4,6-triyl)tribenzaldehyde (TZ) in 12 M acetic acid aqueous solution/mesitylene/DMAC (1:9:1, *v*/*v*/*v*) at 110 °C for 3 days produced the large-pore *L*-DBP-TZ COF (yield: 75%). Notably, the Boc protecting groups were removed in situ during the synthesis of both *L*-DBP-BTA COF and *L*-DBP-TZ COF, enabling a one-step, straightforward construction of pyrrolidine-functionalized chiral COFs. It is worth noting that the previously reported synthetic approaches for pyrrolidine-containing chiral COFs or metal−organic frameworks typically require additional Boc-deprotection steps under harsh conditions (e.g., high temperature or strong acids) [11,38–42], which usually complicate the synthesis, reduce yields, and compromise crystallinity and chiral integrity of the COFs. In contrast, our method eliminates the need for post-synthetic deprotection, directly yielding pyrrolidine-functionalized chiral COFs with relatively high crystallinity in a single step. This strategy provides a simplified and efficient route to the construction of chiral COFs bearing accessible pyrrolidine catalytic sites.

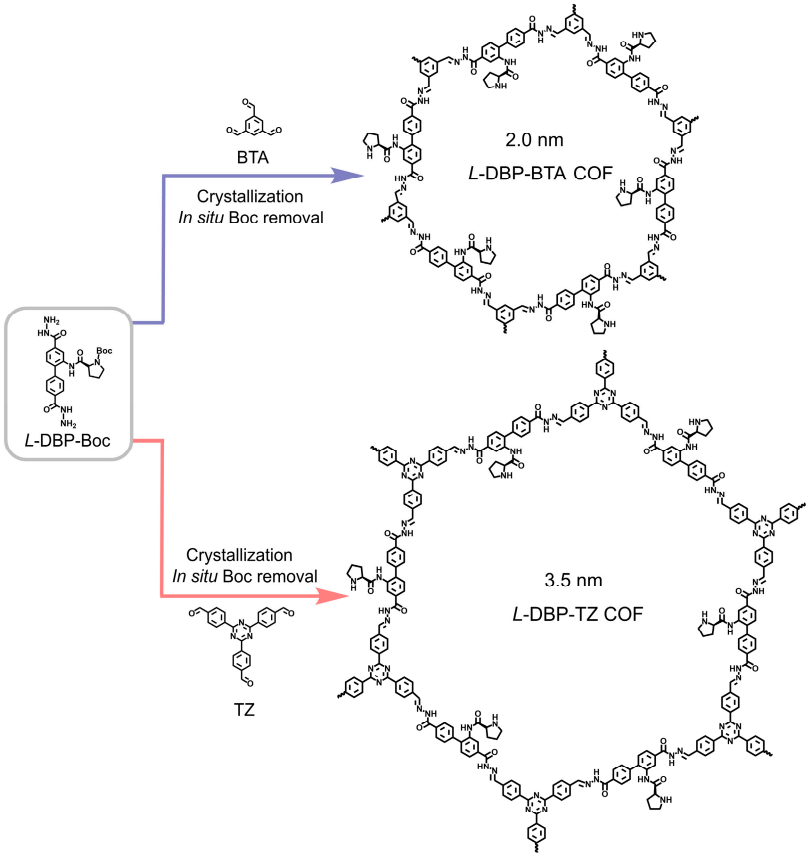


Figure 1. Schematic illustration of the synthesis of chiral *L*-DBP-BTA COF and *L*-DBP-TZ COF.

2.2. Structural Characterization of Chiral COFs

The crystalline structures of the synthesized *L*-DBP-BTA COF and *L*-DBP-TZ COF were characterized by powder X-ray diffraction (PXRD) analysis. As shown in Figure 2a (blue

curve), the PXRD pattern of *L*-DBP-BTA COF exhibited an intense diffraction peak at 2.9°, along with weaker peaks at 4.7° and 26.3°, which could be assigned to the (100), (200), and (001) crystallographic planes, respectively. Similarly, the PXRD profile of *L*-DBP-TZ COF (Figure 2d, red curve) displayed a prominent peak at 2.1° corresponding to the (100) facet, with additional weaker reflections at 4.2° and 26.0°, attributable to the (200) and (001) facets. To elucidate their structural configurations, Materials Studio simulations were performed for both *L*-DBP-BTA COF (Figure 2b,c) and *L*-DBP-TZ COF (Figure 2e,f), considering two plausible packing modes, that is, AA stacking and AB stacking. The experimental PXRD patterns of *L*-DBP-BTA COF and *L*-DBP-TZ COF (Figures 2a and 2d, respectively) aligned well with the simulated patterns derived from the AA-stacking model. Consequently, Pawley refinement was conducted based on the AA-stacking model to obtain optimized unit cell parameters (*L*-DBP-BTA COF: a = b = 37.98 Å, c = 3.563 Å; *L*-DBP-TZ COF: a = b = 52.21 Å, c = 3.545 Å). The refined PXRD patterns displayed great agreement with the experimental data, as evidenced by the low final factors (*L*-DBP-BTA COF: R_{wp} = 3.79%, R_p = 2.91%; *L*-DBP-TZ COF: R_{wp} = 3.66%, R_p = 2.85%), further confirming the AA-stacked crystalline frameworks of the obtained chiral COFs.

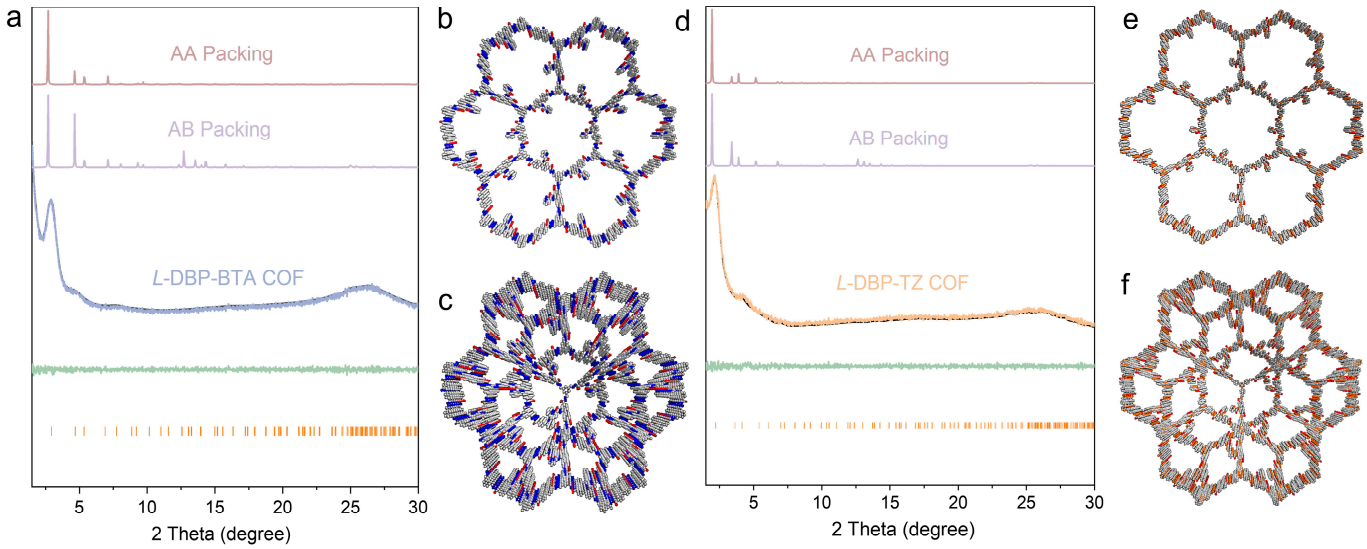


Figure 2. (**a**) PXRD patterns of *L*-DBP-BTA COF: experimental (blue curve), refined from AA-stacking model (black curve), and their difference profile (green curve). (**b**) AA-stacking structure of *L*-DBP-BTA COF. (**c**) AB-stacking structure of *L*-DBP-BTA COF. (**d**) PXRD patterns of *L*-DBP-TZ COF: experimental (red curve), refined from AA-stacking model (black curve), and their difference profile (green curve). (**e**) AA-stacking structure of *L*-DBP-TZ COF. (**f**) AB-stacking structure of *L*-DBP-TZ COF. Orange ticks indicate Bragg positions.

Fourier-transform infrared spectroscopy (FT-IR) analysis confirmed the successful formation of chiral *L*-DBP-BTA COF and *L*-DBP-TZ COF. Compared to the monomers, the FT-IR spectra of both chiral COFs exhibited significant attenuation of amino (3200–3500 cm^{-1}) and aldehyde (1694 cm^{-1}) stretching, while displaying a characteristic C=N stretching vibration at ~1614 cm^{-1}, confirming the formation of imine bonds in the COFs (Figures S1 and S2). Notably, the absence of C-O-C vibrational peaks at ~1254 cm^{-1} in both COFs indicated the complete removal of Boc protecting groups during COF synthesis [42]. Solid-state ^{13}C cross-polarization magic-angle spinning (CP/MAS) NMR spectroscopy provided additional structural verification (Figure 3a,b). The spectra revealed distinct imine carbon signals at ~164 ppm for *L*-DBP-BTA COF and ~163 ppm for *L*-DBP-TZ COF, further evidencing the C=N linkage formation. Characteristic peaks at 170, 62/61, 48, 30, and 23/22 ppm could be assignable to the proline moieties of these chiral

COFs. Besides, in comparison to the reported Boc-containing chiral COFs, the absence of signals at approximately 29, 81, and 155 ppm in the ^{13}C CP/MAS NMR spectra of both *L*-DBP-BTA and *L*-DBP-TZ COFs further confirmed the successful Boc deprotection during COF formation [43]. Thermogravimetric analysis (TGA) demonstrated exceptional thermal stability under a nitrogen atmosphere, with decomposition temperatures of 305 °C for *L*-DBP-BTA COF and 320 °C for *L*-DBP-TZ COF (Figure 3c,d). The slight weight loss below 190 °C for these chiral COFs could be attributed to the departure of the guest solvents in the pore channels, while the absence of weight loss between 190–280 °C provided further evidence for in situ Boc removal during the crystallization of chiral COFs [11]. Chemical stability measurements revealed that the FT-IR spectra of *L*-DBP-BTA and *L*-DBP-TZ COFs remained unchanged and their crystallinity basically maintained after 3-day exposure to H_2O, EtOH, DMF, TBME (tert-butyl methyl ether), DCM, and ACN at room temperature (Figures S3–S6), confirming robust framework integrity of the obtained chiral COFs under diverse conditions.

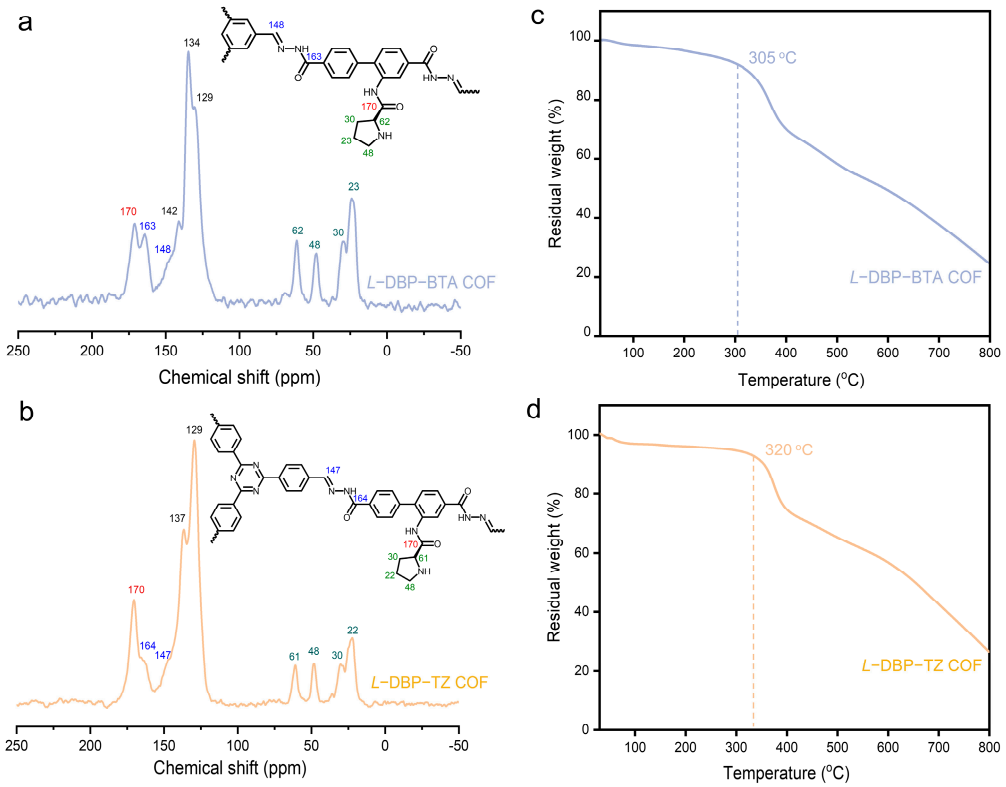


Figure 3. (**a**) Solid-state ^{13}C CP/MAS NMR spectrum of *L*-DBP-BTA COF. (**b**) Solid-state ^{13}C CP/MAS NMR spectrum of *L*-DBP-TZ COF. (**c**) TGA profile of *L*-DBP-BTA COF. (**d**) TGA profile of *L*-DBP-TZ COF.

To evaluate the pore structures of both *L*-DBP-BTA and *L*-DBP-TZ COFs, nitrogen adsorption–desorption measurements were carried out at 77 K and the results were given in Figure 4a,b. When utilizing the Brunauer–Emmett–Teller (BET) model, the surface area values were determined to be 32 $m^2\ g^{-1}$ for *L*-DBP-BTA COF (Figure S7) and 41 $m^2\ g^{-1}$ for *L*-DBP-TZ COF (Figure S8). The observed low BET surface areas might be assignable to the relatively low crystallinity of these COFs and the residual guest solvents trapped in the pore channels via strong hydrogen-bonding interactions [44]. Pore size distribution profiles derived from quenched solid density functional theory (QSDFT) calculations indicated predominant pore diameters of 2.0 nm (Figure 4c) for *L*-DBP-BTA COF and 3.6 nm for *L*-DBP-TZ COF (Figure 4d), which were in great agreement with the theoretically predicted pore sizes (2.0 nm for *L*-DBP-BTA COF and 3.5 nm for *L*-DBP-TZ COF). Scanning electron

microscopy (SEM) analysis revealed distinct morphological features for the synthesized chiral COFs. The *L*-DBP-BTA COF adopted an irregular nanoparticle morphology (Figure 4e), whereas the *L*-DBP-TZ COF possessed a well-defined nanofibrillar architecture (Figure 4f).

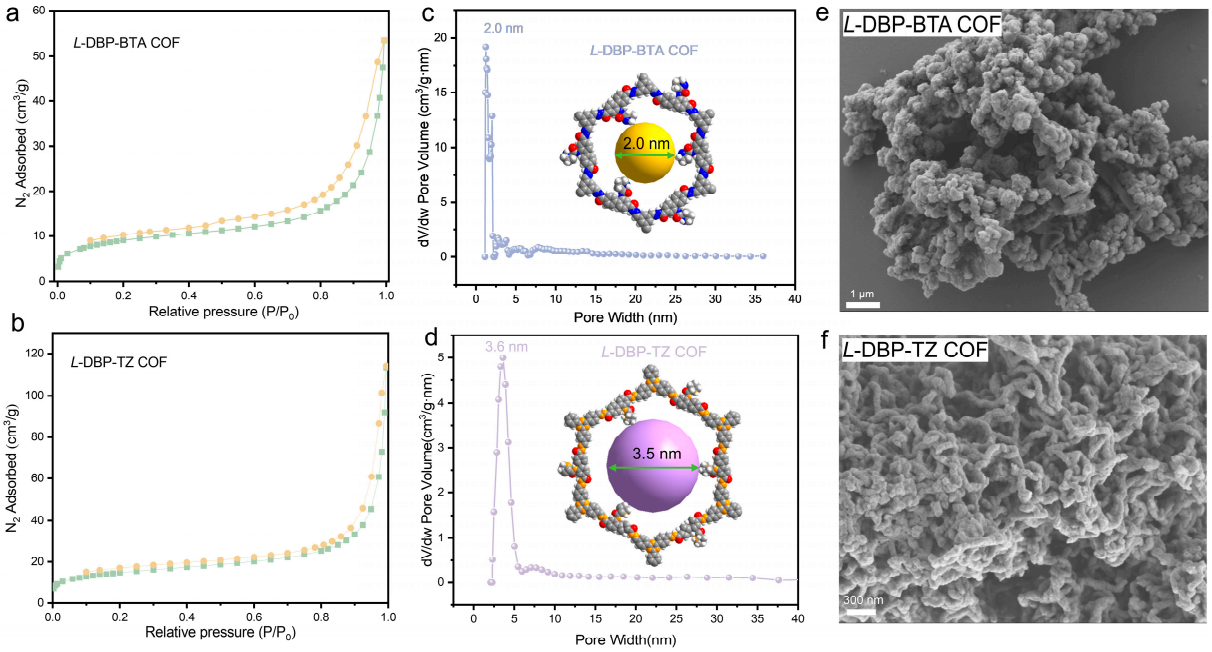


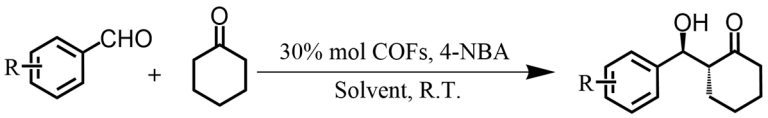
Figure 4. (**a**) N_2 adsorption (green) and desorption (yellow) isotherm curves of *L*-DBP-BTA COF measured at 77 K. (**b**) N_2 adsorption (green) and desorption (yellow) isotherm curves of *L*-DBP-TZ COF at 77 K. (**c**) Pore size distribution profile of *L*-DBP-BTA COF. (**d**) Pore size distribution profile of *L*-DBP-TZ COF. (**e**) SEM image of *L*-DBP-BTA COF. (**f**) SEM image of *L*-DBP-TZ COF.

2.3. Impact of Pore Size on Asymmetric Catalytic Performance in Chiral COFs

The chiral *L*-DBP-BTA and *L*-DBP-TZ COFs both incorporated identical pyrrolidine chiral catalytic moieties, yet feature different pore sizes. This observation prompted us to investigate the influence of pore size on the asymmetric catalytic performance of chiral COFs. We focused our investigation on the asymmetric aldol condensation, a transformative carbon–carbon bond-forming reaction that serves as a cornerstone for constructing chiral centers in pharmaceutical intermediates and fine chemicals [44,45]. To systematically study the structure–activity relationship between pore size and catalytic performance, both *L*-DBP-BTA COF (pore size: 2.0 nm) and *L*-DBP-TZ COF (pore size: 3.5 nm) were employed as heterogeneous catalysts for the asymmetric aldol condensation of cyclohexanone with 4-nitrobenzaldehyde as model substrates. Initially, the catalytic activity of *L*-DBP-TZ COF was investigated utilizing various additives (Table S1). The results showed that low reaction yield (29%) and enantioselectivity (35%) were achieved when using 4-toluenesulfonic acid as an additive. The use of acetic acid and trifluoroacetic acid (TFA) as additives could enhance the ee values (61–64%) but with still low yields (25–30%). In contrast, when 4-nitrobenzoic acid (4-NBA) was used as an additive, the yield (78%) and enantioselectivity (66%) of the reaction were significantly improved. Therefore, 4-NBA was chosen as the optimal additive for the catalytic reaction. We then screened pure organic solvents such as DCM, ACN, DMF, TBME, and EtOH for asymmetric catalysis, however, unsatisfactory yields (23–47%) and enantioselectivity (49–64%) were obtained (Table S2). Further investigation indicated that the mixed system of organic solvents and water could significantly enhance the catalytic efficiency of *L*-DBP-TZ COF, with good reaction activity and enantioselectivity when using DMF/H_2O (10:1, *v*/*v*) as the solvents (entries 1–5 in Table 1). Thus, various ratios of DMF/H_2O were used to investigate the impact of water

on catalytic performance of *L*-DBP-TZ COF and the results showcased that the reaction yields (65 to 90%) and enantioselectivity (62 to 72%) improved as the water ratio increased (entries 5–8 in Table 1). Interestingly, when pure water was used as the solvent, *L*-DBP-TZ COF achieved the highest yield of 98% and an ee value of 78% (entry 9 in Table 1). It was postulated that water might aid in hydrolyzing the reaction intermediate, contributing to improved catalytic performance in the aldol reaction [8,46].

Table 1. Asymmetric aldol reactions catalyzed by *L*-DBP-TZ COF and *L*-DBP-BTA COF.



Entry [a]	Catalyst	R	Solvent	t/d	Yield/% [b]	ee/% [c]	Syn/Anti [d]
1 [e]	*L*-DBP-TZ COF	4-NO_2	DCM:H_2O (10:1)	4	55	60	1:3.4
2 [e]	*L*-DBP-TZ COF	4-NO_2	ACN:H_2O (10:1)	4	43	60	1:3.0
3 [e]	*L*-DBP-TZ COF	4-NO_2	TBME:H_2O (10:1)	4	60	63	1:3.2
4 [e]	*L*-DBP-TZ COF	4-NO_2	EtOH:H_2O (10:1)	4	43	53	1:1.4
5 [e]	*L*-DBP-TZ COF	4-NO_2	DMF:H_2O (10:1)	4	65	62	1:2.0
6 [f]	*L*-DBP-TZ COF	4-NO_2	DMF:H_2O (10:3)	4	78	66	1:3.3
7 [g]	*L*-DBP-TZ COF	4-NO_2	DMF:H_2O (3:10)	4	87	68	1:3.3
8 [h]	*L*-DBP-TZ COF	4-NO_2	DMF:H_2O (1:10)	4	90	72	1:4.2
9	*L*-DBP-TZ COF	4-NO_2	H_2O	3	98	78	1:5.2
10 [i]	*L*-DPD	4-NO_2	H_2O	3	97	89	1:6.4
11	*L*-DBP-TZ COF	3-NO_2	H_2O	3	81	69	1:3.8
12	*L*-DBP-TZ COF	2-NO_2	H_2O	3	41	60	1:2.0
13	*L*-DBP-BTA COF	4-NO_2	H_2O	3	58	50	1:5.1
14	*L*-DBP-BTA COF	3-NO_2	H_2O	3	36	46	1:2.2
15	*L*-DBP-BTA COF	2-NO_2	H_2O	3	17	45	1:2.1

[a] Reaction conditions: aldehyde (0.10 mmol), cyclohexanone (0.3 mL), *L*-DBP-BTA or *L*-DBP-TZ COFs (0.03 mmol chiral centers), 4-nitrobenzoic acid (0.03 mmol), and solvent (1 mL), react at room temperature. [b] Separation yield. [c,d] Determined by chiral HPLC. [e] Organic solvent/H_2O (1 mL/0.1 mL). [f] DMF/H_2O (1 mL/0.3 mL). [g] DMF/H_2O (0.3 mL/1 mL). [h] DMF/H_2O (0.1 mL/1 mL). [i] Catalyzed by 0.03 mmol *L*-DPD as the homogeneous counterpart.

For comparison, we used a Boc-deprotected chiral ester termed *L*-DPD (Scheme S1) as the homogeneous counterpart of the COF catalyst and evaluated its catalytic ability under identical conditions. The results demonstrated that the aldol reaction catalyzed by *L*-DBP-TZ COF achieved a yield comparable to that of *L*-DPD (entry 10 in Table 1), albeit with a lower ee value. Subsequently, catalytic performance of *L*-DBP-BTA COF was conducted under the same reaction conditions. It was worth noting that the reaction yields and enantioselectivity of *L*-DBP-TZ COF were superior to those of *L*-DBP-BTA COF, whether under pure organic solvents (Table S2) or mixed solvents of water and

organic solvents (Tables 1 and S3). When using pure water as the solvent, *L*-DBP-BTA COF could only achieve a yield of 58% and an ee value of 50% (entry 13 in Table 1). Remarkably, in comparison to the small-pore *L*-DBP-BTA COF, the large-pore *L*-DBP-TZ COF demonstrated a 1.69-fold increase in reaction yield and a 1.56-fold enhancement in enantioselectivity under the same tested conditions. This result further confirmed that *L*-DBP-TZ COF with larger pore size might facilitate rapid diffusion of reactants, allowing easier access to more pyrrolidine catalytic active sites and thereby enhancing the catalytic efficiency of the asymmetric aldol reaction [47]. Under optimal conditions, we further investigated the adaptability of different substrates of nitrobenzaldehyde and expanded the application scope of aldol condensation reactions. Under the catalysis of *L*-DBP-TZ COF, the aldol condensation reaction between cyclohexanone and 3-nitrobenzaldehyde afforded the desired product in 81% yield with 69% ee (entry 11 in Table 1). In contrast, the use of *L*-DBP-BTA COF as a catalyst only achieved 36% yield and 46% ee (entry 14 in Table 1). Furthermore, when the substrate was switched to 2-nitrobenzaldehyde (entries 12 and 15 in Table 1), the yields of both chiral COF catalysts decreased significantly (*L*-DBP-TZ COF: 41%; *L*-DBP-BTA COF: 17%) due to the steric hindrance of the ortho-nitro group, while the enantioselectivity remained at a moderate level (60% and 45% ee, respectively). These results clearly demonstrate that when different positional isomers of nitrobenzaldehyde were employed as substrates, the larger-pore *L*-DBP-TZ COF consistently exhibited superior catalytic performance compared to the smaller-pore *L*-DBP-BTA COF (Figure 5).

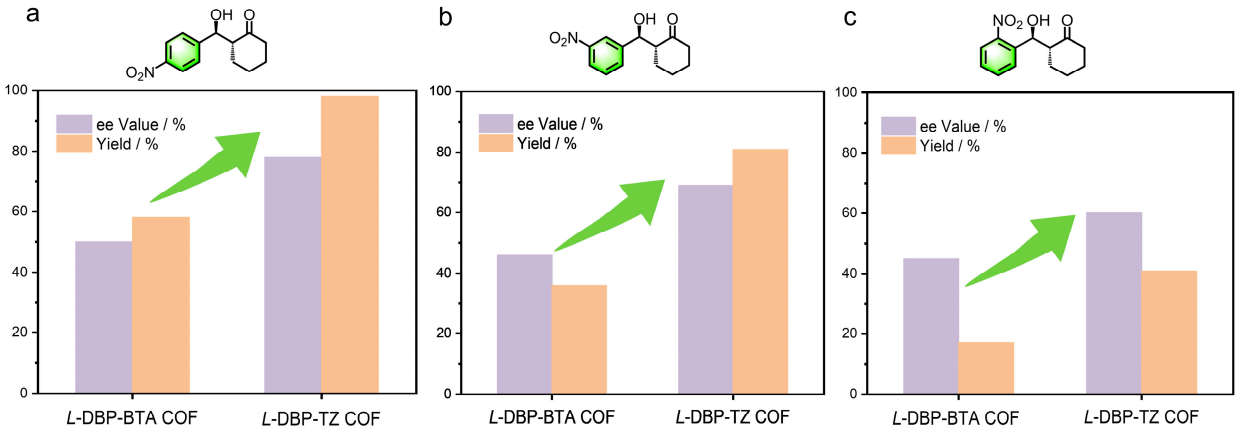


Figure 5. Comparison of asymmetric aldol condensation catalytic performance of chiral *L*-DBP-BTA and *L*-DBP-TZ COFs with different pore sizes. (**a**) Asymmetric aldol reaction of 4-nitrobenzaldehyde and cyclohexanone catalyzed by *L*-DBP-BTA and *L*-DBP-TZ COFs. (**b**) Asymmetric aldol reaction of 3-nitrobenzaldehyde and cyclohexanone catalyzed by *L*-DBP-BTA and *L*-DBP-TZ COFs. (**c**) Asymmetric aldol reaction of 2-nitrobenzaldehyde and cyclohexanone catalyzed by *L*-DBP-BTA and *L*-DBP-TZ COFs.

The aforementioned catalytic performance demonstrated that the large-pore chiral COF outperformed its small-pore analogue in both catalytic activity and stereoselectivity for asymmetric aldol reactions in water, highlighting the critical role of pore size in asymmetric catalysis. Although the mechanism underlying the enhanced catalytic performance of the large-pore chiral COF has not been fully confirmed and further studies are needed, we propose the following potential explanations. The larger pore size of *L*-DBP-TZ COF (3.5 nm) facilitated efficient mass transfer of substrate molecules, allowing more reactants to simultaneously access the pore channels while enabling smooth diffusion of products out of the pores (Figure 6). This enhanced both the reaction rate and enantioselectivity of the asymmetric catalysis. In contrast, for the *L*-DBP-BTA chiral COF with the smaller pore size (2.0 nm), most catalytic centers were embedded within the pore walls, potentially leading

to partial blockage of active sites and reduced accessibility for catalytic reactions [47,48]. Therefore, the large-pore chiral COF afforded greater spatial exposure of chiral active sites within the pore channels, facilitating substrate–catalyst interactions and reducing steric hindrance, which might account for the enhanced catalytic performance of the large-pore *L*-DBP-TZ COF. As a heterogeneous catalyst, we also investigated the recyclability of chiral *L*-DBP-TZ COF. After each catalytic reaction, the solid chiral *L*-DBP-TZ COF catalyst could be readily recovered by centrifugation, washed with MeOH and DCM, and dried under vacuum at 60 °C for subsequent catalytic runs under identical reaction conditions. Remarkably, even after three catalytic cycles, the reaction maintained high yield (94%) and ee value (76%), as illustrated in Figure 7 and Table S4. The minimal decrease in both catalytic activity and enantioselectivity after three cycles demonstrated that the obtained *L*-DBP-TZ COF represented an ideal chiral catalyst for asymmetric aldol condensation reactions. The superior recyclability of the large-pore *L*-DBP-TZ COF catalyst relative to its homogeneous counterpart (*L*-DPD) further highlighted the heterogeneous advantage of this chiral COF catalyst.

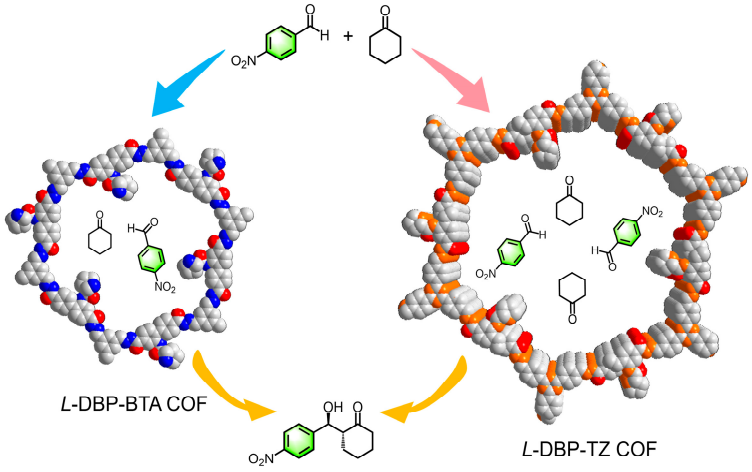


Figure 6. Chiral *L*-DBP-BTA and *L*-DBP-TZ COFs with different pore sizes as catalysts for asymmetric aldol condensation reactions.

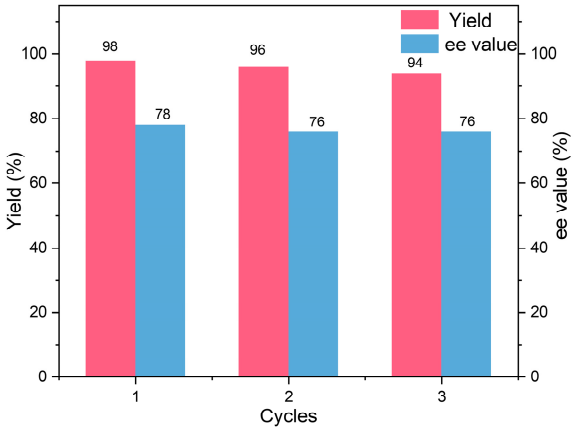


Figure 7. The recycling test of *L*-DBP-TZ COF in the asymmetric aldol reaction.

3. Materials and Methods

3.1. Materials and Instruments

4,4′,4″-(1,3,5-Triazine-2,4,6-triyl) tribenzaldehyde (TZ) was purchased from Shanghai Kylpharm Co., Ltd. (Shanghai, China) Analytical column TZ1 (250 × 4.6 mm, 5 μm) was kindly provided by Guangdong Longsmall Biochemical Technology Co., Ltd. (Guangzhou,

China), which was packed with amylose tris(3,5-dimethylphenylcarbamate)-coated silica gel. Other materials were reagent grade obtained from commercial sources and used directly without further purification. Elemental analyses for C, H, and N were performed on a German Elementar vario EL CUBE (Elementar Analysensysteme GmbH, Hanau, Germany). Powder X-ray diffraction (PXRD) patterns were measured on a Japanese Science Ultima IV X-ray powder diffractometer (Rigaku, Tokyo, Japan) using Cu Kα (λ = 1.5406 Å) radiation. Liquid chromatography-mass spectrometry (LC–MS) determination was conducted on an Agilent 1260–6460 instrument (Agilent, Santa Clara, CA, USA) or a Shimadzu LCMS-2020 instrument (Shimadzu, Kyoto, Japan). Proton and carbon nuclear magnetic resonance (^{1}H NMR and ^{13}C NMR) spectra were acquired on a Bruker Avance NEO 600 MHz spectrometer (Bruker, Karlsruhe, Germany) using tetramethylsilane as the internal standard at room temperature. The solid-state ^{13}C cross-polarization magic-angle spinning (CP-MAS) spectra were collected on a Bruker AVANCE III 400 WB MHz spectrometer (Bruker, Karlsruhe, Germany) at a MAS rate of 10 kHz. Fourier transform infrared spectroscopy (FT-IR) spectra were performed on a Spectrum Two FT-IR Spectrometer (PerkinElmer, Waltham, MA, USA) in the scope of 4000–500 cm^{-1} by using KBr pellets. Thermogravimetric analysis (TGA) was determined using a thermogravimetric analyzer (Netzsch TG 209 F3, Selb, Germany) under a nitrogen atmosphere at a heating rate of 10 °C/min. Nitrogen adsorption−desorption isotherms were measured at 77 K using an American Mike ASAP 2460 surface area and porosity analyzer (Micromeritics, Atlanta, GA, USA). Scanning electron microscopy (SEM) images were carried out on a Carl Zeiss Gemini 500 field emission scanning electron microscope (Carl Zeiss AG, Oberkochen, Germany). The enantiomeric excess (ee) values were determined by HPLC on a Shimadzu LC-20 ADXR system (Shimadzu, Kyoto, Japan) with a TZ1 analytical column.

3.2. Synthesis of the Precursors

3.2.1. Dimethyl 2-Amino-[1,1′-biphenyl]-4,4′-dicarboxylate (1)

3-amino-4-bromobenzoic acid methyl ester (2.76 g, 9 mM), 4-methoxycarbonylphenylboronic acid (2.43 g, 13.5 mM), K_2CO_3 (6.0 eq, 2.70 g), and $Pd(PPh_3)_4$ (0.25 eq, 0.75 g) were added into a pressure resistant bottle. Then a deoxygenated mixture of 1,4-dioxane/H_2O = 4/1 (*v*/*v*) was added to the pressure resistant bottle in an argon atmosphere. After stirring the reaction mixture at 100 °C for 24 h, water was added and extracted with dichloromethane. The combined organic phases were washed with water, dried over Na_2SO_4, and then concentrated under vacuum. Purification was carried out by column chromatography on silica gel using 1:8 EtOAc/hexane as eluent to obtain compound 1 as white crystals (yield: 88%). ^{1}H NMR (600 MHz, DMSO-d_6): δ = 8.04 (d, 2H), 7.60 (d, 2H), 7.43 (s, 1H), 7.23 (s, 1H), 7.13 (d, 1H), 5.24 (s, 2H), 3.83 (d, 6H).

3.2.2. Dimethyl(*S*)-2-(1-(tert-butoxycarbonyl)pyrrolidine-2-carboxamido)-[1,1′-biphenyl]-4,4′-dicarboxylate (2)

To a solution of N-Boc-*L*-proline (2.47 g, 11.48 mmol) and compound 1 (2.2 g, 7.7 mmol) in dichloromethane (DCM, 50 mL), N,N-dicyclohexylcarbodiimide (DCC, 2.84 g, 13.75 mmol) was added. The reaction mixture was stirred at room temperature over 24 h. After that, the mixture was added to H_2O and extracted with DCM. The combined organic phases were washed with H_2O, dried over Na_2SO_4, and concentrated in vacuo. The product was purified by column chromatography over silica gel using 1:3 EtOAc/hexane as the eluent to give the targeted compound 2 (yield: 76%). ^{1}H NMR (600 MHz, DMSO-d_6): δ = 9.60 (d, 1H), 8.16 (d, 1H), 8.05 (d, 2H), 7.89 (d, 1H), 7.59 (m, 3H), 4.13 (m, 1H), 3.89 (s, 6H), 3.27 (m, 2H), 1.36 (s, 9H).

3.2.3. *L*-DPD

Compound 2 (200 mg, 0.41 mmol) was suspended in DCM (4.0 mL) and cooled in an ice bath, then trifluoroacetic acid (TFA, 0.65 mL) was added dropwise. The reaction mixture was allowed to warm to room temperature and stirred for 2 h. Afterward, the mixture was re-cooled to 0 °C, quenched with a saturated $NaHCO_3$ aqueous solution and extracted with DCM (3 × 10 mL). The organic layer was washed with brine, dried over Na_2SO_4, and concentrated under reduced pressure to give *L*-DPD as a white solid (yield: 86%). ^{1}H NMR (600 MHz, DMSO-d_6): δ = 10.30 (s, 1H), 8.73 (s, 1H), 8.10 (m, 2H), 7.81 (s, 1H), 7.60 (m, 2H), 7.47 (m, 1H), 3.91 (d, 6H), 3.83 (m, 1H), 2.89 (m, 1H), 2.68 (m, 1H), 2.53 (m, 1H), 2.07 (m, 1H), 1.82 (m, 1H), 1.68 (m, 2H). ^{13}C NMR (150 MHz, DMSO-d_6): δ = 172.40, 166.38, 166.22 158.98, 142.40, 137.03, 135.37, 130.97, 130.24, 130.02, 129.80, 129.67, 125.70, 123.13, 119.18, 116.20, 60.66, 55.37, 52.77, 46.65, 40.55, 40.34, 40.13, 39.92, 39.71, 39.51, 39.30, 31.72, 30.36, 25.66. LC-MS: *m*/*z* calcd for $C_{21}H_{22}N_2O_5$ $[M + H]^+$: 383.16, found: 383.27.

3.2.4. *L*-DBP-Boc

A mixture solution of hydrazine hydrate (69 mmol, 3.6 mL) and compound 2 (6.9 mmol, 3.3 g) in EtOH solution (50 mL) was refluxed for 24 h, then cooled to room temperature and refrigerated overnight. The formed white crystals of *L*-DBP-Boc were collected by filtration, washed with cold EtOH, and dried in vacuum (yield: 79%). ^{1}H NMR (600 MHz, DMSO-d_6): δ = 9.87 (d, 2H), 9.47 (d, 2H), 8.01 (d, 1H), 7.90 (d, 2H), 7.88 (d, 1H), 7.73 (d, 1H), 7.45 (m, 3H), 4.53 (s, 4H), 4.13 (m, 1H), 3.25 (m, 2H), 2.50 (m, 1H), 2.04 (m, 3H), 1.71 (m, 3H), 1.34 (d, 9H). ^{13}C NMR (150 MHz, DMSO-d_6): δ = 171.86, 171.59, 165.95, 165.66, 154.26, 153.77, 141.47, 141.17, 139.12, 138.36, 135.35, 135.19, 133.64, 132.65, 130.60, 129.06, 127.62, 127.46, 125.60, 124.45, 79.29, 79.13, 60.39, 47.17, 31.00, 29.99, 28.53, 24.30, 23.49. LC-MS: *m*/*z* calcd for $C_{24}H_{30}N_6O_5$ $[M + H]^+$: 483.24, found: 483.20.

3.3. Synthesis of the Chiral COFs

3.3.1. *L*-DBP-BTA COF

A microwave tube was charged with BTA (3.24 mg, 0.02 mmol), *L*-DBP-Boc (14.5 mg, 0.03 mmol), mesitylene (0.6 mL), 1,4-dioxane (0.2 mL) and aqueous acetic acid (0.1 mL, 6 M). After being degassed through three freeze-pump-thaw cycles and then sealed under vacuum, the tube was heated at 110 °C for 3 days. The resulting precipitate was isolated by filtration, washed with DMF, THF, methanol, and acetone then dried under vacuum at 100 °C overnight to offer a pale-yellow solid of chiral *L*-DBP-BTA COF (yield: 72%). Further purification of *L*-DBP-BTA COF was washed by Soxhlet extractions with THF for 24 h, dried under vacuum at 80 °C. Elemental analysis: calcd for $C_{25}H_{22}N_6O_3$: C, 66.07; H, 4.88; N, 18.49%. Found: C, 60.77; H, 5.30; N, 14.49%.

3.3.2. *L*-DBP-TZ COF

A microwave tube was charged with TZ (7.9 mg, 0.02 mmol), *L*-DBP-Boc (14.5 mg, 0.03 mmol), DMAC (0.1 mL), mesitylene (0.9 mL), and aqueous acetic acid (0.1 mL, 12 M). After being degassed through three freeze-pump-thaw cycles and then sealed under vacuum, the tube was heated at 110 °C for 3 days. The resulting precipitate was isolated by filtration, washed with DMF, THF, methanol, and acetone then dried under vacuum at 100 °C overnight to offer a pale-yellow solid of chiral *L*-DBP-TZ COF (yield: 75%). Further purification of *L*-DBP-TZ COF was washed by Soxhlet extractions with THF for 24 h, dried under vacuum at 80 °C. Elemental analysis: calcd for $C_{35}H_{28}N_8O_3$: C, 69.07; H, 4.64; N, 18.41%. Found: C, 64.79; H, 5.27; N, 14.46%.

3.4. Experimental Procedure for Asymmetric Aldol Reactions

In a 10 mL vial containing the chiral COF catalyst (0.03 mmol based on the catalytic chiral centers), aldehyde (0.1 mmol) and 4-nitrobenzoic acid (0.03 mmol) were added to 1.0 mL water and 0.3 mL cyclohexanone. The mixture was stirred for 3–4 days at room temperature. After the reaction (monitored by TLC) was completed, the chiral COF catalyst was isolated by centrifugation and thoroughly washed with DCM for 3 times. The combined organic phases were evaporated under vacuum to give the crude products. Purification by silica gel column chromatography (PE/EtOAc = 3/1) afforded the corresponding aldol product. The ee value was determined using HPLC on a TZ1 analytical column. The yield was the isolated yield.

3.5. The Procedure for Recycled Experiments

The recyclability of *L*-DBP-TZ COF was tested in the asymmetric aldol reaction by using cyclohexanone and 4-nitrobenzaldehyde as the substrates. After each cycle, *L*-DBP-TZ COF was recovered by centrifugation, and washed with DCM (3 × 5 mL), MeOH (with 2% of Et_3N) (3 × 5 mL), H_2O (3 × 5 mL), THF (1 × 6 mL), and MeOH (1 × 6 mL), respectively. The resultant chiral COF powder was dried under vacuum at room temperature and then used for the next catalytic cycle.

4. Conclusions

In summary, we have achieved a facile one-step synthesis of pyrrolidine-functionalized hydrazone-linked chiral *L*-DBP-BTA and *L*-DBP-TZ COFs. While both COFs possessed identical pyrrolidine catalytic moieties, their distinct pore sizes (2.0 nm vs 3.5 nm) enabled systematic investigation of pore dimension effects on asymmetric catalysis. Remarkably, the large-pore *L*-DBP-TZ COF demonstrated superior catalytic performance in asymmetric aldol reactions, achieving exceptional yield (98%) and enantioselectivity (78% ee). Compared to the small-pore *L*-DBP-BTA COF, *L*-DBP-TZ COF exhibited 1.69-fold higher reaction yield and 1.56-fold enhanced enantioselectivity. The *L*-DBP-TZ COF with larger pore size exhibited excellent catalytic performance, mainly attributed to the fact that the larger pore structure was more conducive to the diffusion and transport of substrates and products, increasing the accessibility of active sites. This study not only provides new ideas for the facile synthesis of pyrrolidine-functionalized chiral COFs, but also reveals the possible structure–activity relationship between the pore size and asymmetric catalytic performance of chiral COFs, offering new insights for the rational design of efficient chiral COF catalysts.

Supplementary Materials: The following supporting information can be downloaded at: https://www.mdpi.com/article/10.3390/catal15070640/s1. Scheme S1: The synthetic routes of *L*-DPD and *L*-DBP-Boc; Scheme S2: Synthesis of chiral *L*-DBP-BTA COF; Scheme S3: Synthesis of chiral *L*-DBP-TZ COF; Figure S1: FT-IR spectra of BTA, *L*-DBP-Boc, *L*-DBP-BTA COF. Figure S2. FT-IR spectra of TZ, *L*-DBP-Boc, *L*-DBP-TZ COF; Figure S3: PXRD patterns of *L*-DBP-TZ COF treated in different solvents for 3 days; Figure S4: FT-IR spectra of *L*-DBP-TZ COF treated in different solvents for 3 days; Figure S5: PXRD patterns of *L*-DBP-BTA COF treated in different solvents for 3 days; Figure S6: FT-IR spectra of *L*-DBP-BTA COF treated in different solvents for 3 days; Figure S7: BET surface area plot for *L*-DBP-BTA COF calculated from the absorption isotherm; Figure S8: BET surface area plot for *L*-DBP-TZ COF calculated from the absorption isotherm; Figure S9: PXRD patterns of *L*-DBP-BTA COF before and after catalysis; Figure S10: PXRD patterns of *L*-DBP-TZ COF before and after catalysis; Table S1: Optimization of the aldol reaction conditions (additive); Table S2: Optimization of the aldol reaction conditions (solvent); Table S3: Optimization of the aldol reaction conditions (solvent); Table S4: Recycle test of *L*-DBP-TZ COF; Figure S11: HPLC traces for the aldol addition reaction products between cyclohexanone and 4-nitrobenzaldehyde (corresponding entry 1 in Table 1); Figure S12: HPLC traces for the aldol addition reaction products between cyclohexanone

and 4-nitrobenzaldehyde (corresponding entry 2 in Table 1); Figure S13: HPLC traces for the aldol addition reaction products between cyclohexanone and 4-nitrobenzaldehyde (corresponding entry 3 in Table 1); Figure S14: HPLC traces for the aldol addition reaction products between cyclohexanone and 4-nitrobenzaldehyde (corresponding entry 4 in Table 1); Figure S15: HPLC traces for the aldol addition reaction products between cyclohexanone and 4-nitrobenzaldehyde (corresponding entry 5 in Table 1); Figure S16: HPLC traces for the aldol addition reaction products between cyclohexanone and 4-nitrobenzaldehyde (corresponding entry 6 in Table 1); Figure S17: HPLC traces for the aldol addition reaction products between cyclohexanone and 4-nitrobenzaldehyde (corresponding entry 7 in Table 1); Figure S18: HPLC traces for the aldol addition reaction products between cyclohexanone and 4-nitrobenzaldehyde (corresponding entry 8 in Table 1); Figure S19: HPLC traces for the aldol addition reaction products between cyclohexanone and 4-nitrobenzaldehyde (corresponding entry 9 in Table 1); Figure S20: HPLC traces for the aldol addition reaction products between cyclohexanone and 4-nitrobenzaldehyde (corresponding entry 10 in Table 1); Figure S21: HPLC traces for the aldol addition reaction products between cyclohexanone and 3-nitrobenzaldehyde (corresponding entry 11 in Table 1); Figure S22: HPLC traces for the aldol addition reaction products between cyclohexanone and 2-nitrobenzaldehyde (corresponding entry 12 in Table 1); Figure S23: HPLC traces for the aldol addition reaction products between cyclohexanone and 4-nitrobenzaldehyde (corresponding entry 13 in Table 1); Figure S24: HPLC traces for the aldol addition reaction products between cyclohexanone and 3-nitrobenzaldehyde (corresponding entry 14 in Table 1); Figure S25: HPLC traces for the aldol addition reaction products between cyclohexanone and 2-nitrobenzaldehyde (corresponding entry 15 in Table 1); Figure S26: ^{1}H NMR spectrum (DMSO-d_6, 298 K, 600 MHz) of compound 1; Figure S27: ^{1}H NMR spectrum (DMSO-d_6, 298 K, 600 MHz) of compound 2; Figure S28: ^{1}H NMR spectrum (DMSO-d_6, 298 K, 600 MHz) of *L*-DPD; Figure S29: ^{13}C NMR spectrum (DMSO-d_6, 298 K, 150 MHz) of *L*-DPD; Figure S30: The LC-MS of *L*-DPD; Figure S31: ^{1}H NMR spectrum (DMSO-d_6, 298 K, 600 MHz) of *L*-DBP-Boc; Figure S32: ^{13}C NMR spectrum (DMSO-d_6, 298 K, 150 MHz) of *L*-DBP-Boc; Figure S33: The LC-MS of *L*-DBP-Boc; Table S5: Fractional atomic coordinates for the unit cell of *L*-DBP-BTA COF with AA-packing; Table S6: Fractional atomic coordinates for the unit cell of *L*-DBP-BTA COF with AB-packing; Table S7: Fractional atomic coordinates for the unit cell of *L*-DBP-TZ COF with AA-packing; Table S8: Fractional atomic coordinates for the unit cell of *L*-DBP-TZ COF with AB-packing.

Author Contributions: Writing—original draft preparation, H.H. and K.Z. Software, Y.Z. Formal analysis, H.C. Data curation, D.C. visualization, S.Z. Writing—review and editing, J.F. and S.C. Project administration, J.F. and S.C. Funding acquisition, S.C. All authors have read and agreed to the published version of the manuscript.

Funding: This research was funded by National Natural Science Foundation of China (Grant No. 22171092), the Guangdong Basic and Applied Basic Research Foundation (Grant No. 2024A1515011117), the Science and Technology Program of Guangzhou (Grant No. 2024A04J2407), and the Special Funds for the Cultivation of Guangdong College Students' Scientific and Technological Innovation (Climbing Program Special Funds. Grant No. pdjh2024a113).

Data Availability Statement: The data that support the findings of this study are available on request from the authors.

Conflicts of Interest: There are no conflicts to declare.

References

1. Han, X.; Yuan, C.; Hou, B.; Liu, L.; Li, H.; Liu, Y.; Cui, Y. Chiral covalent organic frameworks: Design, synthesis and property. *Chem. Soc. Rev.* **2020**, *49*, 6248–6272. [CrossRef] [PubMed]
2. Kang, X.; Stephens, E.R.; Spector-Watts, B.M.; Li, Z.; Liu, Y.; Liu, L.; Cui, Y. Challenges and opportunities for chiral covalent organic frameworks. *Chem. Sci.* **2022**, *13*, 9811–9832. [CrossRef] [PubMed]
3. Liu, G.; Sheng, J.; Zhao, Y. Chiral covalent organic frameworks for asymmetric catalysis and chiral separation. *Sci. China Chem.* **2017**, *60*, 1015–1022. [CrossRef]

4. Wu, X.; Han, X.; Zhang, J.; Jiang, H.; Hou, B.; Liu, Y.; Cui, Y. Metal–and covalent organic frameworks threaded with chiral polymers for heterogeneous asymmetric catalysis. *Organometallics* **2019**, *38*, 3474–3479. [CrossRef]
5. Hu, H.; Yan, Q.; Ge, R.; Gao, Y. Covalent organic frameworks as heterogeneous catalysts. *Chin. J. Catal.* **2018**, *39*, 1167–1179. [CrossRef]
6. Dong, Y.; Yin, C.F.; Kan, J.L.; Chang, C.R.; Ma, J.P.; Liu, J.B.; Dong, Y.B. Au-Acyclic Diaminocarbene-Linked Homochiral Covalent Organic Frameworks: Synthesis and Asymmetric Catalytic Application. *Chem. Mater.* **2024**, *37*, 473–479. [CrossRef]
7. Kang, X.; Cheng, C.; Chen, X.; Dong, J.; Liu, Y.; Cui, Y. Three-Dimensional Homochiral Covalent Organic Frameworks with Intrinsic Chiral qzd Topology. *J. Am. Chem. Soc.* **2024**, *146*, 8407–8416. [CrossRef]
8. Li, J.; Zhang, K.; Tang, X.; Yang, X.; Chen, H.; Zheng, S.; Fan, J.; Xie, M.; Zhang, W.; Li, X.; et al. Primary Amine-Functionalized Chiral Covalent Organic Framework Enables High-Efficiency Asymmetric Catalysis in Water. *ACS Appl. Mater. Interfaces* **2024**, *16*, 59379–59387. [CrossRef]
9. Yu, J.; Yang, G.; Gao, M.L.; Wang, H.; Jiang, H.L. Chiral Ligand-Decorated Rhodium Nanoparticles Incorporated in Covalent Organic Framework for Asymmetric Catalysis. *Angew. Chem. Int. Ed.* **2024**, *63*, e202412643. [CrossRef]
10. Zhang, J.; Han, X.; Wu, X.; Liu, Y.; Cui, Y. Multivariate Chiral Covalent Organic Frameworks with Controlled Crystallinity and Stability for Asymmetric Catalysis. *J. Am. Chem. Soc.* **2017**, *139*, 8277–8285. [CrossRef]
11. Zhang, K.; Zheng, Y.; Chen, H.; Cai, D.; Tang, X.; Zheng, S.; Cai, S. Dimensionality control of chiral covalent organic frameworks for enhanced asymmetric catalysis. *Chem. Eng. J.* **2025**, *515*, 163613. [CrossRef]
12. Liu, P.; Dai, W.; Shen, X.; Shen, X.; Zhao, Y.; Liu, J.J. Recent Advances in the Utilization of Chiral Covalent Organic Frameworks for Asymmetric Photocatalysis. *Molecules* **2024**, *29*, 5006. [CrossRef]
13. Han, X.; Zhang, J.; Huang, J.; Wu, X.; Yuan, D.; Liu, Y.; Cui, Y. Chiral induction in covalent organic frameworks. *Nat. Commun.* **2018**, *9*, 1294. [CrossRef] [PubMed]
14. Wu, X.; Han, X.; Xu, Q.; Liu, Y.; Yuan, C.; Yang, S.; Liu, Y.; Jiang, J.; Cui, Y. Chiral BINOL-Based Covalent Organic Frameworks for Enantioselective Sensing. *J. Am. Chem. Soc.* **2019**, *141*, 7081–7089. [CrossRef] [PubMed]
15. Yuan, C.; Fu, S.; Yang, K.; Hou, B.; Liu, Y.; Jiang, J.; Cui, Y. Crystalline C-C and C=C Bond-Linked Chiral Covalent Organic Frameworks. *J. Am. Chem. Soc.* **2021**, *143*, 369–381. [CrossRef] [PubMed]
16. Yue, J.Y.; Song, L.P.; Shi, Y.H.; Zhang, L.; Pan, Z.X.; Yang, P.; Tang, B. Chiral ionic covalent organic framework as an enantioselective fluorescent sensor for phenylalaninol determination. *Anal. Chem.* **2023**, *95*, 11078–11084. [CrossRef]
17. Yuan, L.; Tang, X.; Zhang, K.; Chen, H.; Yang, X.; Fan, J.; Cai, S. Construction of a Defective Chiral Covalent Organic Framework for Fluorescence Recognition of Amino Acids. *Chem.-Asian J.* **2024**, *19*, e202400753. [CrossRef]
18. Song, Q.; Yang, J.; Zheng, K.; Zhang, T.; Yuan, C.; Yuan, L.M.; Hou, X. Chiral Memory in Dynamic Transformation from Porous Organic Cages to Covalent Organic Frameworks for Enantiorecognition Analysis. *J. Am. Chem. Soc.* **2024**, *146*, 7594–7604. [CrossRef]
19. Zhang, K.; Cai, S.L.; Yan, Y.L.; He, Z.-H.; Lin, H.M.; Huang, X.L.; Zheng, S.R.; Fan, J.; Zhang, W.G. Construction of a hydrazone-linked chiral covalent organic framework-silica composite as the stationary phase for high performance liquid chromatography. *J. Chromatogr. A* **2017**, *1519*, 100–109. [CrossRef]
20. Zhang, S.; Zheng, Y.; An, H.; Aguila, B.; Yang, C.X.; Dong, Y.; Xie, W.; Cheng, P.; Zhang, Z.; Chen, Y.; et al. Covalent Organic Frameworks with Chirality Enriched by Biomolecules for Efficient Chiral Separation. *Angew. Chem. Int. Ed.* **2018**, *57*, 16754–16759. [CrossRef]
21. Xu, J.; Feng, G.; Ao, D.; Li, X.; Li, M.; Lei, S.; Wang, Y. Functional Covalent Organic Frameworks Microspheres Synthesized by Self-Limited Dynamic Linker Exchange for Stationary Phases. *Adv. Mater.* **2024**, *36*, 2406256. [CrossRef] [PubMed]
22. Zhang, S.; Zheng, Y.; An, H.; Aguila, B.; Yang, C.X.; Dong, Y.; Ma, S. A Chiral COFs Membrane for Enantioselective Amino Acid Separation. *Angew. Chem. Int. Ed.* **2025**, *64*, e202417088. [CrossRef]
23. Zhang, X.; Hou, B.; Li, Z.; Fu, S.; Liu, S.; Jia, L.; Cui, Y. Highly Enantioselective Transportation Across Liquid Membranes Mediated by Porous Covalent Organic Frameworks. *Angew. Chem. Int. Ed.* **2025**, *64*, e202419916. [CrossRef]
24. Fu, S.; Qin, G.; Dong, J.; Yuan, C.; Liu, Y.; Yuan, L.M.; Cui, Y. Construction of chiral crown ethers in robust covalent organic frameworks for electrochromatographic enantioseparation. *Natl. Sci. Rev.* **2024**, *11*, 256. [CrossRef]
25. Yuan, C.; Wang, Z.; Xiong, W.; Huang, Z.; Lai, Y.; Fu, S.; Dong, J.; Duan, A.; Hou, X.; Yuan, L.M.; et al. Cyclodextrin Incorporation into Covalent Organic Frameworks Enables Extensive Liquid and Gas Chromatographic Enantioseparations. *J. Am. Chem. Soc.* **2023**, *145*, 8956–18967. [CrossRef]
26. Chen, H.; Gu, Z.G.; Zhang, J. Chiral-Induced Ultrathin Covalent Organic Frameworks Nanosheets with Tunable Circularly Polarized Luminescence. *J. Am. Chem. Soc.* **2022**, *144*, 7245–7252. [CrossRef] [PubMed]
27. Tang, X.; Liao, X.; Cai, X.; Wu, J.; Wu, X.; Zhang, Q.; Yan, Y.; Zheng, S.; Jiang, H.; Fan, J.; et al. Self-Assembly of Helical Nanofibrous Chiral Covalent Organic Frameworks. *Angew. Chem. Int. Ed.* **2023**, *62*, e202216310. [CrossRef]

28. Tang, X.; Zhang, K.; Xue, R.; Zheng, Y.; Chen, S.; Zheng, S.; Fan, J.; Zhang, Y.; Ye, W.; Zhang, W.; et al. Self-Standing Chiral Covalent Organic Framework Thin Films with Full-Color Tunable Guest-Induced Circularly Polarized Luminescence. *Angew. Chem. Int. Ed.* **2024**, *63*, e202413171. [CrossRef]
29. Gu, Q.; Zha, J.; Chen, C.; Wang, X.; Yao, W.; Liu, J.; Zhang, Q. Constructing chiral covalent-organic frameworks for circularly polarized light detection. *Adv. Mater.* **2024**, *36*, 2306414. [CrossRef]
30. Tang, X.; Zha, J.; Wu, X.; Tong, J.; Gu, Q.; Zhang, K.; Zhang, Y.; Zheng, S.; Fan, J.; Zhang, W.; et al. Construction of Chiral Covalent Organic Frameworks Through a Linker Decomposition Chiral Induction Strategy for Circularly Polarized Light Detection. *Angew. Chem. Int. Ed.* **2025**, *64*, e202413675. [CrossRef]
31. Jing, S.M.; Gu, Z.G.; Zhang, J. Chiral Cross-Linked Covalent Organic Framework Films for Highly Sensitive Circularly Polarized Luminescence Probing. *J. Am. Chem. Soc.* **2025**, *147*, 8948–8958. [CrossRef] [PubMed]
32. Wang, L.K.; Zhou, J.J.; Lan, Y.B.; Ding, S.Y.; Yu, W.; Wang, W. Divergent synthesis of chiral covalent organic frameworks. *Angew. Chem. Int. Ed.* **2019**, *131*, 9543–9547. [CrossRef]
33. Liu, S.; Li, W.L.; Zhang, J.P. Revealing the potential application of chiral covalent organic frameworks in CO_2 adsorption and separation. *New J. Chem.* **2020**, *44*, 95–101. [CrossRef]
34. Zhuo, S.; Zhang, X.; Luo, H.; Wang, X.; Ji, Y. The application of covalent organic frameworks for chiral chemistry. *Macromol. Rapid. Comm.* **2020**, *41*, 2000404. [CrossRef] [PubMed]
35. Liu, Q.; Li, Z.; Sun, J.; Lan, Y.; Hu, J.; Xiao, Y.; Gao, D. Recent Advance in the Synthesis and Applications of Chiral Covalent Organic Frameworks. *J. Sep. Sci.* **2025**, *48*, e70101. [CrossRef]
36. Weng, W.; Guo, J. Chiral Covalent Organic Framework Films with Enhanced Photoelectrical Performances. *J. Am. Chem. Soc.* **2024**, *146*, 13201–13209. [CrossRef] [PubMed]
37. Zhang, J.; Han, X.; Wu, X.; Liu, Y.; Cui, Y. Chiral DHIP- and Pyrrolidine-Based Covalent Organic Frameworks for Asymmetric Catalysis. *ACS Sustain. Chem. Eng.* **2019**, *7*, 5065–5071. [CrossRef]
38. Zhang, K.; Tang, X.; Yang, X.; Wu, J.; Guo, B.; Xiao, R.; Xie, Y.; Zheng, S.; Jiang, H.; Fan, J.; et al. Raising the Asymmetric Catalytic Efficiency of Chiral Covalent Organic Frameworks by Tuning the Pore Environment. *ACS Appl. Mater. Interfaces* **2024**, *16*, 10661–10670. [CrossRef]
39. Xu, H.S.; Ding, S.Y.; An, W.K.; Wu, H.; Wang, W. Constructing Crystalline Covalent Organic Frameworks from Chiral Building Blocks. *J. Am. Chem. Soc.* **2016**, *138*, 11489–11492. [CrossRef]
40. He, T.; Liu, R.; Wang, S.; On, I.K.W.; Wu, Y.; Zhao, Y. Bottom–Up Design of Photoactive Chiral Covalent Organic Frameworks for Visible-Light-Driven Asymmetric Catalysis. *J. Am. Chem. Soc.* **2023**, *145*, 18015–18021. [CrossRef]
41. Lun, D.J.; Waterhouse, G.I.N.; Telfer, S.G. A General Thermolabile Protecting Group Strategy for Organocatalytic Metal−Organic Frameworks. *J. Am. Chem. Soc.* **2011**, *133*, 5806–5809. [CrossRef]
42. Wang, Y.; Zheng, Y.; Chen, H.; Chen, X.; Zhang, K.; Liang, W.; Cai, S. Construction of a spherical chiral covalent organic framework for efficient asymmetric aldol catalysis. *J. Solid State Chem.* **2025**, *348*, 125350. [CrossRef]
43. Chen, G.; Lan, H.H.; Cai, S.L.; Sun, B.; Li, X.L.; He, Z.H.; Zhang, W.G. Stable hydrazone-linked covalent organic frameworks containing *O*,*N*,*O*′-chelating sites for Fe (III) detection in water. *ACS Appl. Mater. Interfaces* **2019**, *11*, 12830–12837. [CrossRef]
44. List, B.; Lerner, R.A.; Barbas, C.F. Proline-Catalyzed Direct Asymmetric Aldol Reactions. *J. Am. Chem. Soc.* **2000**, *122*, 2395–2396. [CrossRef]
45. Trost, B.M.; Brindle, C.S. The direct catalytic asymmetric aldol reaction. *Chem. Soc. Rev.* **2010**, *39*, 1600–1632. [CrossRef] [PubMed]
46. Meso, G.; Gregorich, D.; Waite, A.J.; Smith, S.; Liu, L.; Cortez, J.; Liu, Y. Organocatalytic Assembly Based on Aromatic Donor–Acceptor Interactions for the Asymmetric Aldol Reaction on Water. *ChemCatChem* **2023**, *15*, e202300012. [CrossRef]
47. Newar, R.; Kalita, R.; Akhtar, N.; Antil, N.; Chauhan, M.; Manna, K. N-Formylation of amines utilizing CO_2 by a heterogeneous metal–organic framework supported single-site cobalt catalyst. *Catal. Sci. Technol.* **2022**, *12*, 6795. [CrossRef]
48. Shan, H.; Zhang, Z.; Jiang, Y.; Cai, D.; Qin, P.; Baeyens, J. Two-dimensional porphyrin-based covalent organic frameworks for heterogeneous photocatalysis: Influence of pore size on photocatalytic performance. *Sep. Purif. Technol.* **2025**, *363*, 132102. [CrossRef]

Disclaimer/Publisher's Note: The statements, opinions and data contained in all publications are solely those of the individual author(s) and contributor(s) and not of MDPI and/or the editor(s). MDPI and/or the editor(s) disclaim responsibility for any injury to people or property resulting from any ideas, methods, instructions or products referred to in the content.